Interface Science

Low-angle boundary engineering for improving high-cycle fatigue property of 430 ferritic stainless steel

Shigeaki Kobayashi[1,*] , Weitao Yang[2,4], Yuuki Tomobe[1], Rei Okada[2], and Sadahiro Tsurekawa[3]

[1] *Division of Mechanical Engineering, Department of Innovative Engineering, Faculty of Engineering, Ashikaga University, Omae 268-1, Ashikaga, Tochigi 326-8558, Japan*

[2] *Department of Information Science and Manufacturing Engineering, Graduate School of Engineering, Ashikaga University, Omae 268-1, Ashikaga, Tochigi 326-8558, Japan*

[3] *Structural Materials, Division of Materials Science and Chemistry, Faculty of Advanced Science and Technology, Kumamoto University, Kumamoto 860-8555, Japan*

[4] *Present address: Shanghai Research Institute of Materials, No.99 Handan Road, Hongkou District, Shanghai, China*

ABSTRACT

Grain boundary engineering (GBE) based on the control of a low-angle grain boundary (LAGB) network was investigated to improve the fatigue property in 430 ferritic stainless steel. The development of a subboundary structure during annealing in a specimen that was cold rolled at a high reduction ratio was evaluated quantitatively by electron backscatter diffraction measurements. The fine subgrain structure with a high fraction of LAGBs (F_L = 54%) was produced with the formation of a sharp {100} and {111} texture by cold rolling to 95% with subsequent annealing at 973 K for 600 s. The LAGBs interconnected to form networks in the GBEed specimen. The kernel average misorientation maps suggest that the dislocation density within the LAGB network was higher than that in the recrystallized grains, particularly near the LAGBs. The high-cycle fatigue property in specimens with different magnitudes of LAGB networks was compared with that in the annealed commercial 430 stainless steel. The kernel average misorientation maps for the post-fatigued GBEed specimen reveal that the dislocation density decreased during cyclic deformation, whereas the fine-grained structure and high fraction of LAGBs were maintained. It was concluded that the grain refinement and introduction of a high fraction of LAGBs can achieve a higher fatigue strength and longer fatigue life for 430 stainless steel.

Address correspondence to E-mail: skoba@ashitech.ac.jp

Springer

Introduction

Ferritic stainless steels have been applied widely as structural materials which required a high corrosion and oxidation resistance, such as in automobile exhaust system parts. Although ferritic stainless steels show a lower corrosion and oxidation resistance than austenitic stainless steels, they provide cost advantages and a low thermal expansion coefficient.

The fatigue fracture of materials dominates the structural component lifetime. The control of fatigue fracture in structural components is important to prevent accidents and reduces the environmental burden. Fatigue fracture in 430 ferritic stainless steel is affected by grain boundaries with a specific character [1, 2]. Fatigue cracks nucleate preferentially at random boundaries, whereas cracks never nucleate at low-angle grain boundaries (LAGBs) [1]. The propagation rate of fatigue cracks decreases when the crack passes across grain boundaries irrespective of the grain boundary character; however, the crack propagation rate is accelerated when cracks propagate along random boundaries [2]. These results suggest that the introduction of a fine-grained structure with a high fraction of LAGBs helps to improve the high-cycle fatigue property in 430 stainless steel.

Many research groups have studied the precise introduction of a high fraction of Σ3 boundaries in face-centered cubic (fcc) metallic materials with a low stacking fault energy, as related to multiple twinning by annealing [3–9]. In twinning-related grain boundary engineering (GBE), the fraction of annealing twin boundaries, namely {111}/Σ3 coincidence site lattice (CSL) boundaries, is increased by cold rolling at a low reduction ratio and with subsequent high-temperature annealing. The control of intergranular degradation phenomena, such as intergranular corrosion [10–14], intergranular stress corrosion cracking [15–21], grain boundary segregation embrittlement [22–24] and fatigue cracking [25–28], has been achieved by twinning-related GBE. Recently, the more precise thermomechanical processing of the GBE was investigated by topological and geometrical approaches, such as by an evaluation of grain boundary plane distribution [29–32], percolation of grain boundary connectivity [12, 13, 33–35] and fractal analysis of grain boundary connectivity [36, 37], although the GBE has been achieved traditionally by controlling the grain boundary character

distribution (GBCD) [38–40]. We demonstrated that intergranular corrosion in SUS316L austenitic stainless steel was controlled when specimens had a lower fractal dimension of random boundary network with a maximum connectivity in the specimen, namely maximum random boundary connectivity (MRBC) [37].

The GBE process for body-centered cubic (bcc) materials has not been established, although some successful achievements on GB microstructure control have been reported for bcc materials that were produced by special processing [41–45]. Watanabe et al. [41, 42] investigated experimentally the relationship between the GBCD and texture type in Fe–6.5 mass% Si polycrystalline ribbons that were produced by rapid solidification and subsequent annealing. They revealed that CSL boundaries with specific Σ-values occurred preferentially depending on the texture type and sharpness [41, 42]. We found that a high fraction of LAGBs was introduced within the oriented grain clusters, namely the local texture in molybdenum polycrystals that was produced by uniaxial compression and subsequent annealing from single crystals with different initial orientations [43, 44]. The fraction of LAGBs in the individual oriented grain cluster depended on their surface orientation. The highest fraction of LAGBs occurred in the {001}-oriented grain cluster. Although a few studies have achieved GBE for bcc materials [39, 46, 47], the effectiveness of GBE for controlling the intergranular degradation phenomena should be demonstrated for many bcc materials.

We evaluated quantitatively the development of a subboundary network, namely a LAGB network during annealing after cold rolling at a high reduction ratio. We aimed to obtain an indication of the grain boundary microstructure control consisting of a fine-grained structure with a high fraction of LAGBs in the 430 ferritic stainless steel. The fatigue property of the 430 stainless steel specimens with different magnitudes of the LAGB network was investigated compared with that in the specimen that was produced by annealing of commercial hot-rolled 430 stainless steel.

Experimental procedure

Specimen preparation

Commercial hot-rolled 430 stainless steel sheet with 25 mm thick was subjected to annealing in air at 1273 K for 64.8 ks (18 h) and subsequent cooling. The annealed 430 stainless steel sheet was cold rolled to 95% in a reduction ratio. The cold-rolled specimens were annealed at 973 K, 993 K, 1023 K, 1073 K and 1123 K for 600 s in a vacuum to prevent the formation of a thick oxidation scale on the specimen surface and then cooled in air.

Specimens for high-cycle fatigue tests were cut from the thermomechanically processed sheet using a spark machine. Figure 1 shows the fatigue specimen shape and dimensions with 10 mm length, 4 mm width and 1.2 mm thickness. The specimen surface was polished mechanically by using emery papers of 320–1500 grade and diamond powder slurry of 0.5 μm in particle size. Thereafter, the surface of the fatigue specimen was polished electrolytically in an electrolytic solution of 23 vol% perchloric acid and 77 vol% acetic acid at a current density of 2.2 mA/mm^2 at 277 K for 20 s.

Evaluation of grain structure and grain boundary microstructure

An X-ray diffractometer (Rigaku RINT 2000) with monochromatic Cu-Kα radiation was used to characterize the orientation distribution in the cold-rolled 430 stainless steel specimen. X-ray diffraction (XRD) measurements ($30° \leq 2\theta \leq 100°$) were carried out at a scanning step of 0.02° at an accelerating voltage of 40 kV and a filament current of 100 mA, with a 1 mm collimator slit.

Scanning electron microscopy (SEM)/electron backscatter diffraction (EBSD) measurements were used to evaluate the grain boundary microstructure in the annealed specimens quantitatively. The SEM/

EBSD measurements were conducted on a FEG-SEM (HITACHI SU-5000) equipped with a TSL's orientation imaging microscopy (OIM) system. The electron beam was scanned with a 0.2–1.0 μm step size at an accelerated voltage of 20 kV and an emission current of 10 μA on a specimen surface. The grain size distribution, grain orientation distribution, kernel average misorientation (KAM) and GBCD in the annealed specimens were determined based on EBSD data. The KAM indicates an average value of misorientation between one measured point and all adjacent measured points. Recent studies have reported that the KAM reflects the plastic strain that results from the geometrically necessary dislocation density [48–50]. The grain boundaries with $3 \leq \Sigma \leq 29$ were defined as low-Σ CSL boundaries, according to previous reports [36–40, 51]. Although the CSL boundaries are not characterized fully by the Σ-value (misorientation angle), experimental evidence has indicated that the CSL boundaries with a Σ-value $\leq \Sigma29$ exhibit a higher resistance to intergranular fatigue fracture and grain boundary degradation than random boundaries. The LAGBs ($\Sigma1$ boundaries) were distinctively evaluated from the other low-Σ CSL boundaries, because we focus on the LAGBs in this study. The GBCD was evaluated from the length fraction for different grain boundary types in individual 430 stainless steel specimens. The magnitude of the LAGB network was evaluated from the total LAGB length per unit area.

High-cycle fatigue tests

High-cycle fatigue tests on the 430 stainless steel specimens were carried out by using a servo-hydraulic machine (Shimadzu, Servopulser EHF-FB10kN-10L) in air at room temperature. The loading direction was kept parallel to the specimen rolling direction. A sinusoidal stress that ranged from 190 MPa to 310 MPa in stress amplitude was applied at a stress ratio of 0.1 and at a frequency of 10 Hz. The range of stress amplitude was smaller than the yield stress of the pre-fatigued specimens and fell into the high-cycle fatigue category.
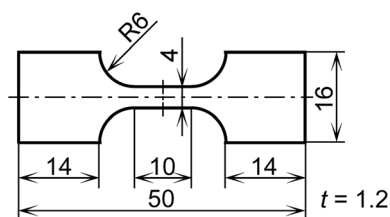

Figure 1 Fatigue specimen shape and dimensions.

Results and discussion

Microstructure in initial annealed specimen and cold-rolled specimen

Figure 2 shows the inverse pole figure (IPF) map and grain boundary (GB) map for the initial 430 stainless steel specimen before cold rolling. Hereafter, this specimen is referred to as the base material (BM) specimen. In the IPF map, the surface orientation of individual grains is shown by distinct colors that correspond to those in the stereo triangle on the right-hand side of the IPF map. The BM specimen had an average grain size of 38 μm, and its surface was weakly oriented to {100}. In the GB map, the grain boundary types are shown by different colors that correspond to those in the color bars on the right of the GB map. The fractions of LAGBs, low-Σ CSL boundaries and random boundaries in the BM specimen were 5%, 6% and 89%, respectively.

Figure 3 shows the XRD profile of the specimen that was cold rolled at a 95% reduction ratio. The specimen surface was sharply oriented to {100} and

Figure 3 XRD profile of specimen subjected to cold rolling at 95% strain.

weakly oriented to {211}, compared with the XRD profile of Fe standard powders. The cold-rolled specimen was kept at 473 K for 200 h to observe the cold-rolled structure in more detail by FEG-SEM/EBSD/OIM analysis. Figure 4 shows the IPF map with the IPFs and the KAM map of the cold-rolled specimen kept at 473 K. Annealing at 473 K for 200 h resulted in a decrease in dislocation density where the EBSD patterns that could be analyzed were obtained. Figure 4 shows that the grains were elongated in the rolling direction and their surface was sharply oriented to {100}. The surface orientation of the elongated {100}-oriented grains changed

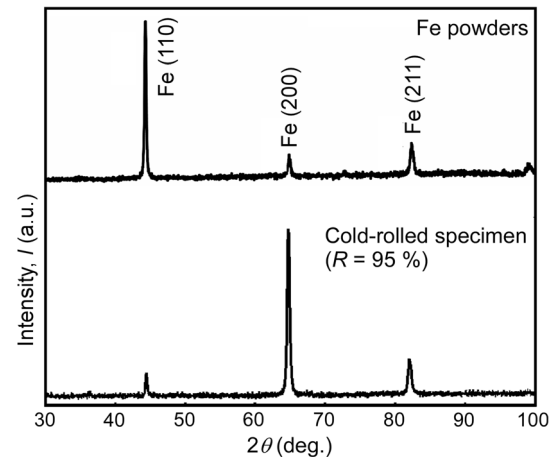**Figure 2** IPF and GB maps for initial 430 stainless steel specimen before cold rolling (BM specimen).
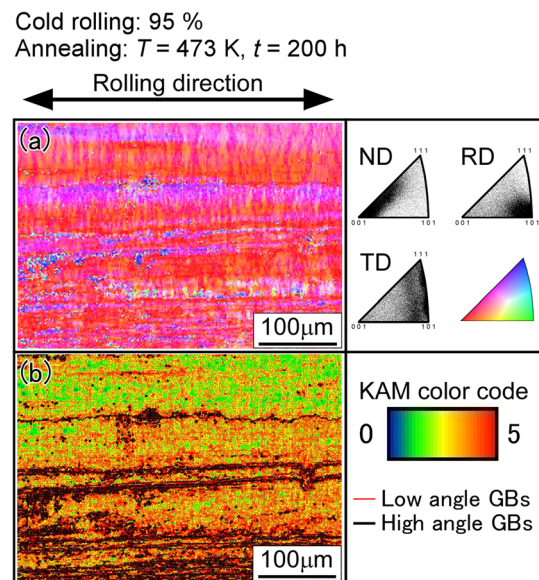

Figure 4 IPF map with IPF and KAM map of cold-rolled specimen kept at 473 K for 200 h.

gradually into {112} near the grain boundaries between the adjoining elongated grains. The KAM map revealed that the elongated {100}-oriented grains maintained a high dislocation density that was introduced by the cold rolling. The areas near the grain boundary between adjacent elongated grains were in a highly strained structure. In general, the {100} plane is one of the final stable orientations of cold rolling in bcc metallic materials, as well as the {111} plane [52–54]. The orientation distribution spread from {112} to {100} is reasonable if we consider the crystal rotation in bcc materials by cold rolling. The surface orientation of 430 ferritic stainless steel can be controlled by the high reduction ratio of cold rolling.

Evolution of grain boundary microstructure by cold rolling and subsequent annealing

Figure 5 shows IPF maps of the 430 stainless steel specimens that were produced by cold rolling of 95% in a reduction ratio and subsequent annealing at 973–1123 K for 600 s. Although the average grain size increased with an increase in annealing temperature, all specimens possessed a fine-grained structure from 1.4 to 6.7 μm in average grain size. The specimens that were annealed at less than 993 K were composed mainly of {100}- and {111}-oriented grains. It appears that the {100}-oriented grains were finer than those with the other surface orientations. The orientation distribution of the specimen surface changed to a random distribution with grain growth.

Figure 5a, b shows that the {111}-oriented grains nucleated preferentially, grew near the {100}-oriented grains and formed a {111} recrystallization texture. The {111} recrystallized grains most likely nucleated at grain boundaries between the elongated {100}-oriented grains in the cold-rolled specimen, because the {111}-oriented grains were observed along the {100}-oriented grain clusters in Fig. 5a. The preferential nucleation and growth of the {111}-oriented recrystallized grains from the {100} cold-rolled texture have been observed also in molybdenum with a bcc structure, which was produced by uniaxial compressive deformation and subsequent annealing [43, 44].

Figure 6 shows the KAM maps of the annealed specimens. The observed areas in these KAM maps

Figure 5 IPF maps of specimens produced by cold rolling of 95% in reduction ratio and subsequent annealing at 973–1123 K for 600 s.
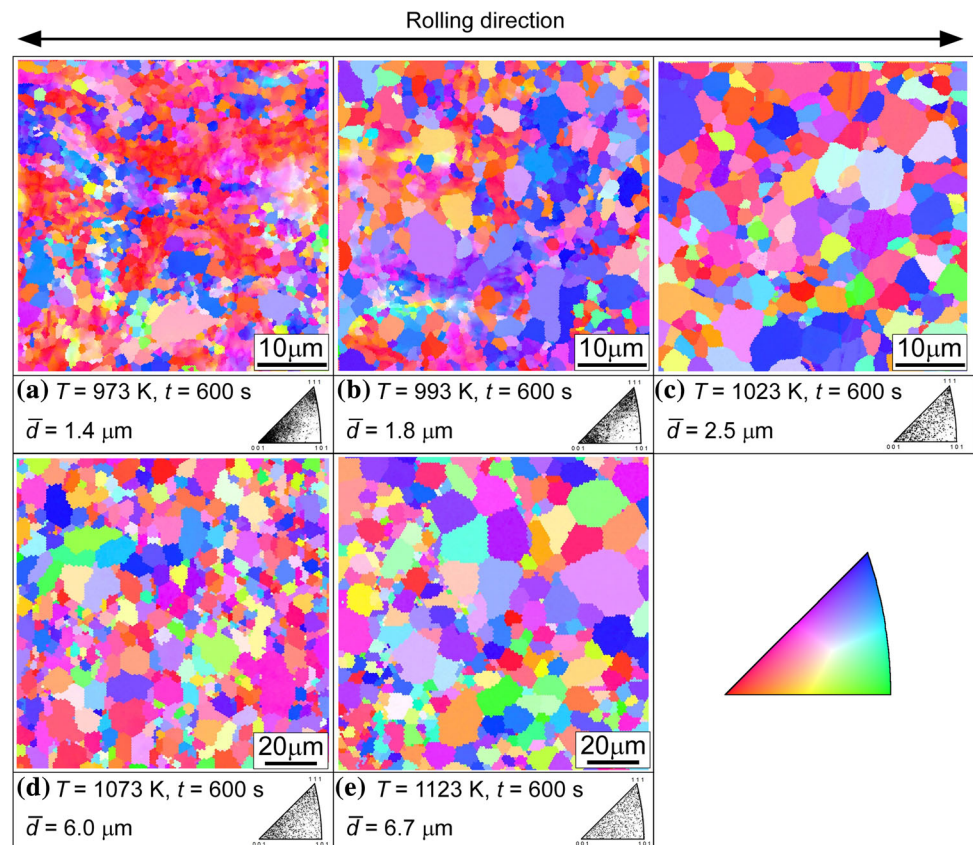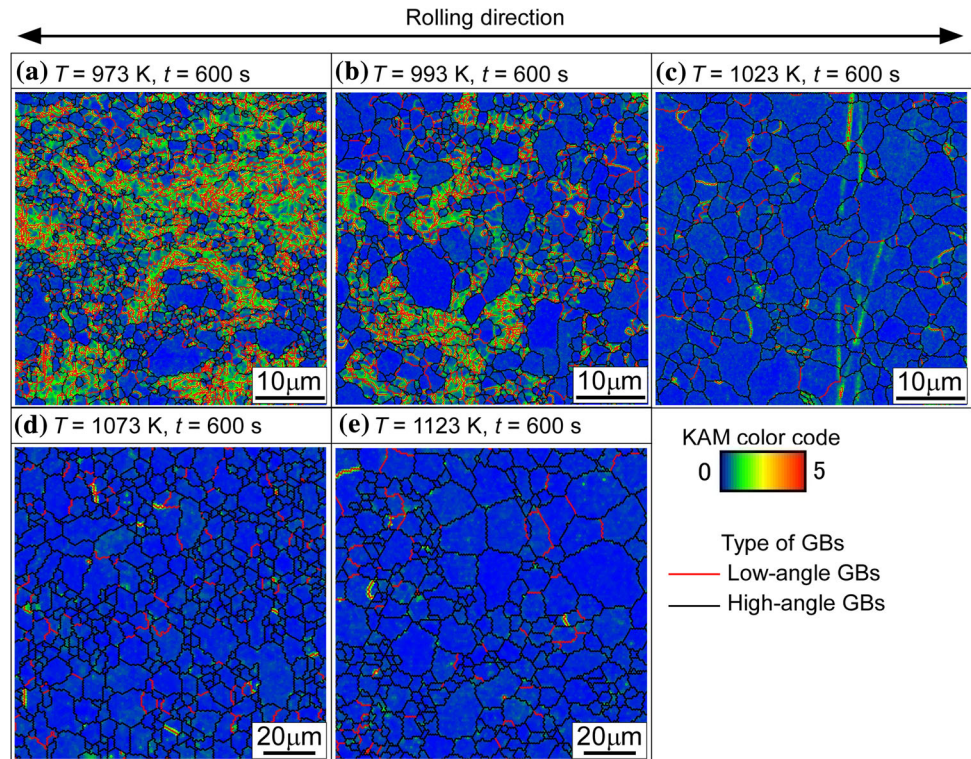
Figure 6 KAM maps of specimens produced by cold rolling of 95% in reduction ratio and subsequent annealing at 973–1123 K for 600 s.

correspond to the areas in the IPF maps in Fig. 5. The colors that were applied to the KAM values correspond to the KAM color codes on the right of Fig. 6. The highly strained areas were distributed in specimens that were annealed at 973 K and 993 K. These strained areas were composed of {100}-oriented grains and contained a high fraction of LAGBs, as shown in Fig. 5. These results suggest that the {100}-oriented grains were subgrains that developed within the {100} rolling texture. Specimens that were annealed above 1023 K had a fully recrystallized structure despite the short annealing time, because they contained no strained areas.

Figure 7 shows the grain size distribution in the specimens that were annealed at different temperatures after cold rolling. For specimens that were annealed at 973 K and 993 K, the grain size distributions for the subgrains and recrystallized grains were evaluated individually from data that were obtained from more than 300 grains in each specimen. In the specimen that was annealed at 973 K for 600 s, the average grain sizes of the subgrains and the recrystallized grains were 1.2 μm and 1.5 μm, respectively. The grain size distribution of the recrystallized grains was kept in a similar range to that of the subgrains. The subgrain size distribution

hardly changed with annealing, even at 993 K. The subgrain structure disappeared in the specimens that were annealed above 1023 K. The grain size distribution suggests that the recrystallized grains showed normal grain growth behavior for all annealing conditions.

Figure 8 shows the GB maps with GBCD and magnitude of the LAGB network for the specimens that were annealed at different temperatures after cold rolling. The specimen with high LAGB fraction of 54% was produced by cold rolling to 95% and subsequent annealing at 973 K for 600 s. Here, the magnitude of the LAGB network in this specimen was $\rho_L = 1335$ mm/mm^2. Although the introduction of a high fraction of CSL boundaries with specific Σ-values was expected by the formation of a sharp {100} and {111} texture as shown by the experimental [41, 42, 55] and theoretical [56–60] studies, the total fraction of low-Σ $(3 \leq \Sigma \leq 29)$ CSL boundaries was 6%. These LAGBs occurred in the {100}-oriented subgrain structure and in the {111} recrystallization texture. Although the specimen that was annealed at 1023 K for 600 s possessed a reasonably high fraction of LAGBs of 16%, the fraction of LAGBs in the fully annealed specimens decreased with an increase in annealing temperature.
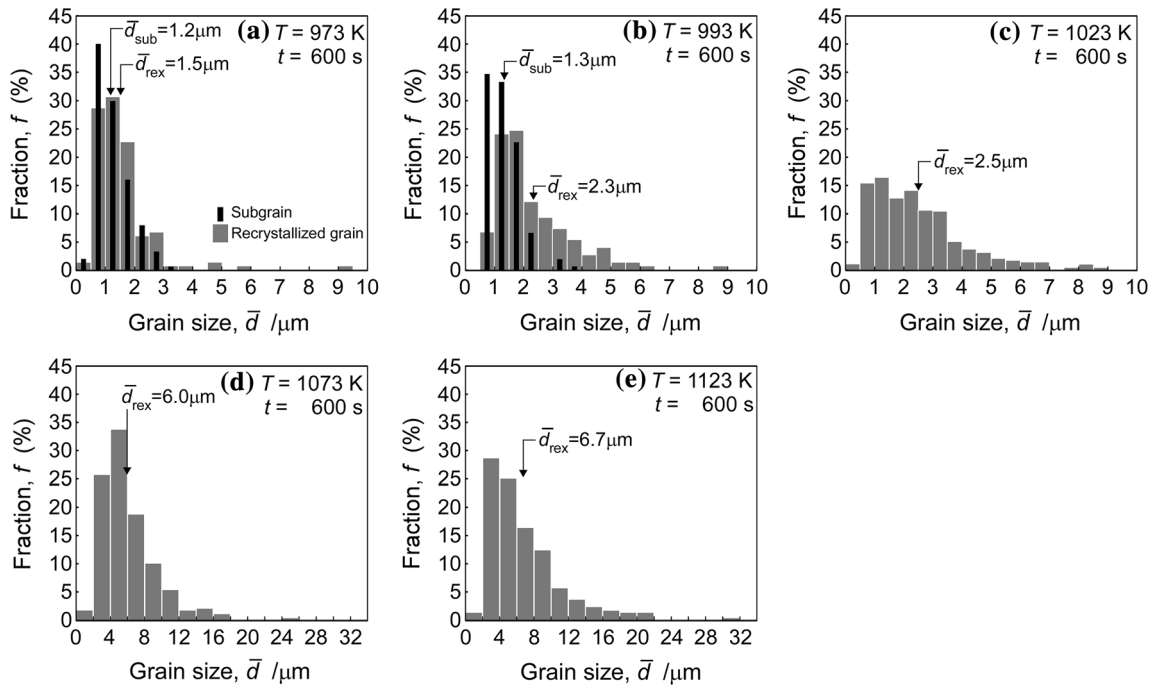
Figure 7 Grain size distribution in specimens produced by cold rolling of 95% in reduction ratio and subsequent annealing at 973–1123 K for 600 s.

Figure 8 GB maps of 430 stainless steel specimens produced by cold rolling of 95% in reduction ratio and subsequent annealing at 973–1123 K for 600 s.
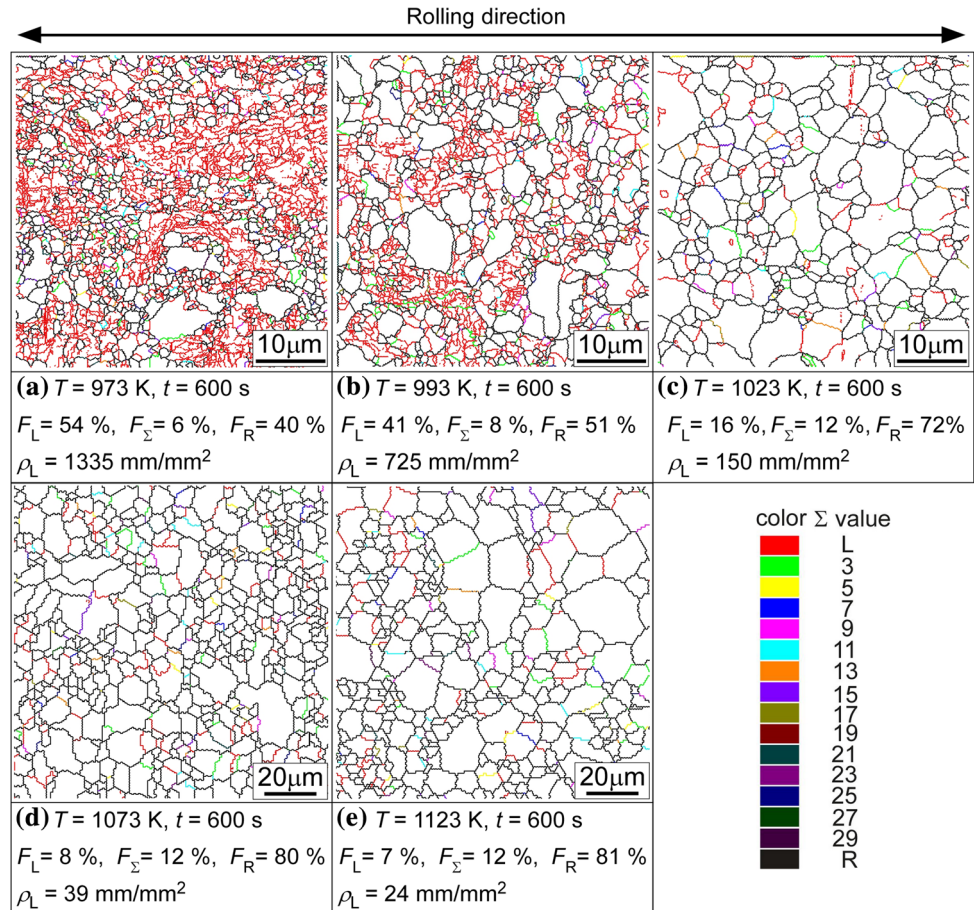
Figure 9 shows the relationship between the magnitude of the LAGB network and the fraction of LAGBs. The values of the magnitude of the LAGB network ρ_L increased in a quadratic function with increasing fraction of LAGBs regardless of whether a subgrain or recrystallized structure.

Effect of LAGB-induced GBE on high-cycle fatigue property in 430 stainless steel

To reveal the effectiveness of the LAGB-induced GBE on the improvement in a high-cycle fatigue property in 430 stainless steel, the high-cycle fatigue property of the specimens with different magnitudes of LAGB networks was compared with the BM specimen with a conventional grain boundary microstructure. The subgrain-structured specimen which possessed a magnitude of LAGB network of 1335 mm/mm^2, an average grain size of 1.4 μm and a total fraction of LAGBs and low-Σ CSL boundaries of 60% was designated as a Type A specimen. The fully recrystallized specimen which possessed a magnitude of LAGB network of 150 mm/mm^2, an average grain size of 2.5 μm and a total fraction of LAGBs and low-Σ CSL boundaries of 28% was designated as a Type B specimen. Here, low-Σ CSL boundaries were evaluated with LAGBs, because low-Σ CSL boundaries show a higher resistance to fatigue crack nucleation and propagation than random boundaries [1, 2].

Figure 10a shows the relationship between the stress amplitude and the number of cycles to fracture, namely the S–N curves for the Type A, Type B and BM specimens. The estimated fatigue limits of the Type A, Type B and BM specimens were 270 MPa,
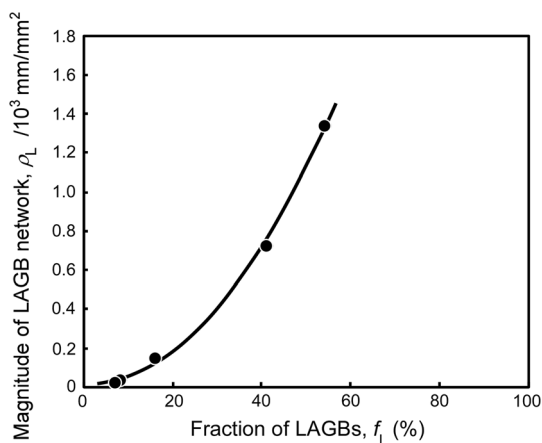
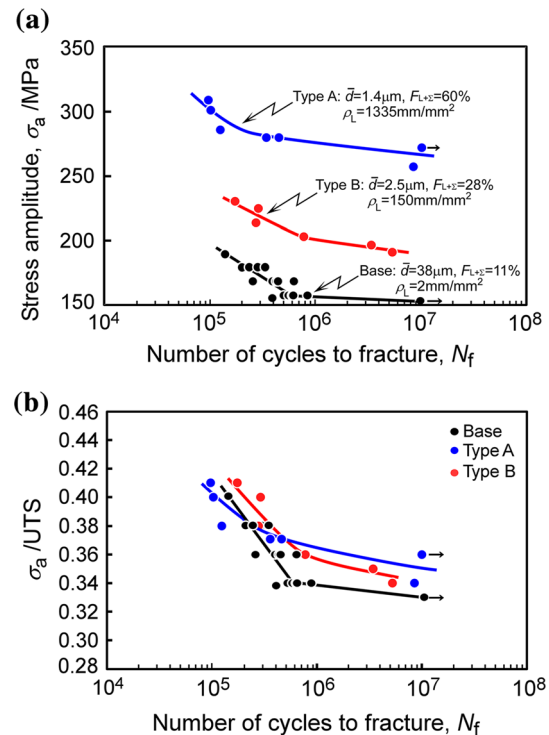**Figure 9** Relationship between magnitude of LAGB network and fraction of LAGBs.

Figure 10 a S–N curves and **b** relationship between stress amplitude normalized by ultimate tensile strength and number of cycles to fracture for GBEed and BM specimens.

185 MPa and 157 MPa, respectively. The Type A specimen with the largest magnitude of LAGB network (the highest total fraction of low-angle and low-Σ CSL boundaries) showed the highest fatigue limit of all the specimens. Although the effect of average grain size on the fatigue properties may have not been fully negligible, it has been reported that the fatigue property was influenced less by the average grain size in the materials with a conventional grain structure [61, 62]. The relationship between the stress amplitude that was normalized by the ultimate tensile strength (UTS) and the number of cycles to fracture is shown in Fig. 10b, because the fatigue limit generally increases with an increase in UTS of materials. The UTSs of the Type A, Type B and BM specimens were 753 MPa, 562 MPa and 464 MPa, respectively. The high tensile strength in the Type A specimen was most likely caused by the fine-grained structure and work hardening owing to residual dislocations in the {100} subgrain structure. The fatigue life at a high stress amplitude level of ∼ 0.38 UTS was almost the same as that between the Type A and Type B specimens. However, the fatigue strength in the Type A specimen became significantly higher

than that in the Type B specimen at the low stress amplitude level below 0.36 UTS. Therefore, it can be concluded that the LAGB-induced GBE was useful for improving the high-cycle fatigue property in the 430 ferritic stainless steel.

Change in microstructure in LAGB-induced GBEed specimen during high-cycle fatigue test

The change in subgrain structure in the Type A specimen during cyclic deformation was observed because detrimental effects of the initial high dislocation density on the fatigue property may be considered. Figure 11 shows the IPF, KAM and GB maps

of the specimen surface ∼ 500 μm from the fracture surface. The specimen was subjected to a cyclic deformation at 279 MPa in stress amplitude and was fractured at a cycle number of 434,099. The IPF map showed that the specimen surface was oriented strongly to {100} and {111}. The surface orientation distribution was hardly changed by cyclic deformation. The post-fatigued specimen maintained an average grain size of 1.4 μm, which is similar to the pre-fatigued specimen. However, areas that were composed of coarsened grains that were surrounded by LAGBs formed in the post-fatigued specimen, as shown by the area (i) in Fig. 11. These coarsened grains reached 5–8 μm in grain size. The fine subgrain structure with an average grain size of ∼ 1 μm

Figure 11 IPF, KAM and GB maps of specimen surface ∼ 500 μm from fracture surface in post-fatigued specimen.
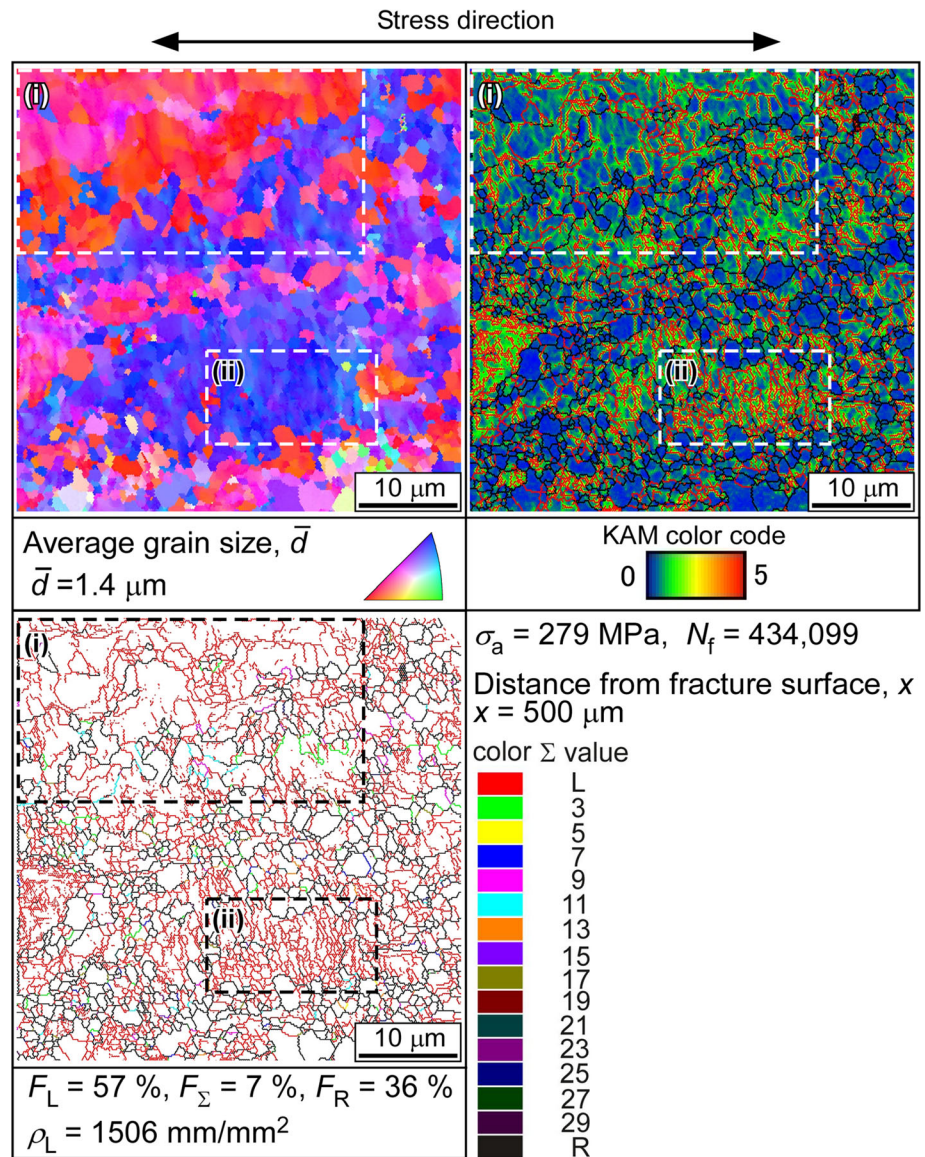
was kept even in the post-fatigued specimen, as shown in area (ii) of Fig. 11. The KAM map (Fig. 11b) shows that the coarse subgrains were divided into some fine subgrains by boundaries with a small misorientation angle below 2°. Although the pre-fatigued specimen included a high density of dislocations in the subgrain interior (Fig. 6a), highly strained areas were distributed only around LAGBs in the post-fatigued specimen.

The GB map (Fig. 11c) reveals that the post-fatigued specimen retained a high fraction of LAGBs (57%) during cyclic deformation. As shown in Fig. 12a, b, the misorientation distribution hardly changed between the pre- and post-fatigued specimens. The post-fatigued specimen included a high fraction of LAGBs with a low misorientation angle below 3°. These results suggest that dislocations in the subgrain interior were not absorbed into LAGBs but were combined and/or disappeared by their interaction to form new LAGBs (subboundaries). Grain coarsening in area (i) seemed to occur by the disappearance of dislocations during cyclic

deformation. A decrease in dislocation density and grain coarsening was observed in the area more than 350 μm from the fracture surface. Although the microstructural changes were significant at the area close to closer to the fracture surface, they resulted mainly from plastic deformation at the final fracture stage rather than from fatigue deformation. It is possible that the strength decreased locally by grain coarsening, and fracture occurred in areas that were composed of coarsened grains.

This work shows that an introduction of a larger-magnitude LAGB network (higher fraction of low-angle boundaries and low-Σ CSL boundaries) resulted in higher fatigue strength in the 430 ferritic stainless steel, because of an inhibition of fatigue crack nucleation and propagation by LAGBs.

Conclusions

GBE based on the control of LAGBs in 430 ferritic stainless steel was investigated by thermomechanical processing. The effectiveness of the LAGB-induced GBE to improve the high-cycle fatigue property was examined by using 430 stainless steel specimens with different magnitudes of LAGB networks and GBCDs. The main conclusions are as follows:

(1) A large LAGB network was formed within the sharp {100} and {111} texture in the specimens that were produced by 95% cold rolling and subsequent annealing at 973 K for a short treatment time of 600 s. LAGB network control within the subgrain structure was one of the possible processes for GBE in bcc metallic materials.

(2) The specimen with a higher fraction of LAGBs and a larger magnitude of LAGB network showed a higher fatigue strength and longer fatigue life. The LAGB-induced GBE can improve the high-cycle fatigue property in 430 ferritic stainless steel.

(3) The average grain size, texture type, GBCD and strain distribution in the pre-fatigued 430 stainless steel specimen hardly changed during the fatigue test. However, areas that were composed of coarsened grains were formed by cyclic deformation. A possible fracture mechanism was proposed based on the
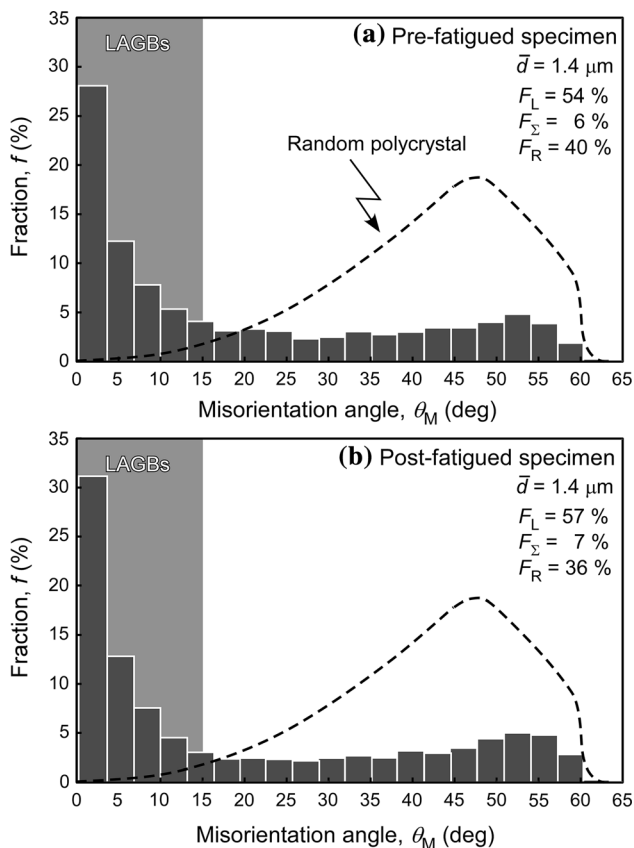

Figure 12 Change in misorientation angle distribution between pre- and post-fatigued specimens.

observation results of grain coarsening in the post-fatigued specimen.

Compliance with ethical standards

Conflict of interest The authors declare that they have no conflict of interest.

References

[1] Yang WT, Kobayashi S, Saito S (2017) Effect of grain boundary character on nucleation of intergranular fatigue cracks in SUS430 ferritic stainless steel. Trans JSME. https://doi.org/10.1299/transjsme.16-00460

[2] Yang WT, Kobayashi S, Saito S (2018) Effect of grain boundary microstructure on fatigue crack propagation in ferritic stainless steel. Trans JSME. https://doi.org/10.1299/transjsme.17-00353

[3] Randle V (1999) Mechanism of twinning-induced grain boundary engineering in low stacking-fault energy materials. Acta Mater 47:4187–4196

[4] Kumar M, Schwartz AJ, King WE (2002) Microstructural evolution during grain boundary engineering of low to medium stacking fault energy fcc materials. Acta Mater 50:2599–2612

[5] Randle V (2004) Twinning-related grain boundary engineering. Acta Mater 52:4067–4081

[6] Randle V, Coleman M (2009) A study of low-strain and medium-strain grain boundary engineering. Acta Mater 57:3410–3421

[7] Akhiani H, Nezakat M, Sanayei M, Szpunar J (2015) The effect of thermo-mechanical processing on grain boundary character distribution in Incoloy 800H/HT. Mater Sci Eng A626:51–60

[8] Barr CM, Leff AC, Demott RW, Doherty RD, Taheri ML (2018) Unraveling the origin of twin related domains and grain boundary evolution during grain boundary engineering. Acta Mater 144:281–291

[9] Prithiv TS, Bhuyan P, Pradhan SK, Sarma VS, Mandal S (2018) A critical evaluation on efficacy of recrystallization vs. strain induced boundary migration in achieving grain boundary engineered microstructure in a Ni-base superalloy. Acta Mater 146:187–201

[10] Lin P, Palumbo G, Erb U, Aust KT (1995) Influence of grain boundary character distribution on sensitization and intergranular corrosion of alloy 600. Scripta Metall Mater 33:1387–1392

[11] Shimada M, Kokawa H, Wang ZJ, Sato YS (2002) Optimization of grain boundary character distribution for intergranular corrosion resistant 304 stainless steel by twin-induced grain boundary engineering. Acta Mater 50:2331–2341

[12] Tsurekawa S, Nakamichi S, Watanabe T (2006) Correlation of grain boundary connectivity with grain boundary character distribution in austenitic stainless steel. Acta Mater 54:3617–3626

[13] Michiuchi M, Kokawa H, Wang ZJ, Sato YS, Sakai K (2006) Twin-induced grain boundary engineering for 316 austenitic stainless steel. Acta Mater 54:5179–5184

[14] Saito S, Kikuchi K, Hamaguchi D, Tezuka M, Miyagi M, Kokawa H, Watanabe S (2012) Corrosion-erosion test of SS316L grain boundary engineering material (GBEM) in lead bismuth flowing loop. J Nucl Mater 431:91–96

[15] Cheung C, Erb U, Palumbo G (1994) Application of grain boundary engineering concepts to alleviate intergranular cracking in Alloy 600 and 690. Mater Sci Eng A185:39–43

[16] Palumbo G, Lehockey EM, Lin P, Erb U, Aust KT (1997) A grain boundary engineering approach to materials reliability. In: Briant CL, Carter CB, Hall EL (eds.) Interfacial engineering for optimized properties, Mat Res Soc Symp Proc, vol. 458, pp. 273–282

[17] Was GS, Thaveeprungsriporn V, Crawford DC (1998) Grain boundary misorientation effects on creep and cracking in Ni-based alloys. JOM 50:44–49

[18] Was GS, Alexandreanu B, Andresen P, Kumar M (2004) Role of coincidence site lattice boundaries in creep and stress corrosion cracking. In: Schuh CA, Kumar M, Carter CB, Randle V (eds.) Mat Res Soc Symp Proc, vol 819, pp. 87–100

[19] Alexandreanu B, Was GS (2006) The role of stress in the efficacy of coincidence site lattice boundaries in improving creep and stress corrosion cracking. Script Mater 54:1047–1052

[20] West EA, Was GS (2009) IGSCC of grain boundary engineered 316L and 690 in supercritical water. J Nucl Mater 392:264–271

[21] Telang A, Gill AS, Tammana D, Wen X, Kumar M, Teysseyre S, Mannava SR, Qian D, Vasudevan VK (2015) Surface grain boundary engineering of alloy 600 for improved resistance to stress corrosion cracking. Mater Sci Eng A648:280–288

[22] Krupp U, Kane WM, Liu A, Dueber O, Laird C, McMahon CJ Jr (2003) The effect of grain-oundary-engineering-type

processing on oxygen-induced cracking of IN718. Mater Sci Eng A349:213–217

[23] Bechtle S, Kumar M, Somerday BP, Launey ME, Ritchie RO (2009) Grain-boundary engineering markedly reduces susceptibility to intergranular hydrogen embrittlement in metallic materials. Acta Mater 57:4148–4157

[24] Kobayashi S, Tsurekawa S, Watanabe T, Palumbo G (2010) Grain boundary engineering for control of sulfur segregation-induced embrittlement in ultrafine-grained nickel. Script Mater 62:294–297

[25] Gao Y, Kumar M, Nalla RK, Ritchie RO (2005) High-cycle fatigue of nickel-based superalloy ME3 at ambient and elevated temperatures: role of grain-boundary engineering. Metall Mater Trans 36A:3325–3333

[26] Gao Y, Stölken JS, Kumar M, Ritchie RO (2007) High-cycle fatigue of nickel-base superalloy René 104 (ME3): interaction of microstructurally small cracks with grain boundaries of known character. Acta Mater 55:3155–3167

[27] Kobayashi S, Nakamura M, Tsurekawa S, Watanabe T (2011) Effect of grain boundary microstructure on fatigue crack propagation in austenitic stainless steel. J Mater Sci 46:4254–4260. https://doi.org/10.1007/s10853-010-5238-1

[28] Kobayashi S, Ogou S, Tsurekawa S (2019) Grain boundary engineering for control of fatigue fracture in 316L austenitic stainless steel. Mater Trans 60:623–630

[29] Rohrer GS, Randle V, Kim C-S, Hu Y (2006) Changes in the five-parameter grain boundary character distribution in α-brass brought about by iterative thermomechanical processing. Acta Mater 54:4489–4502

[30] Randle V, Jones R (2009) Grain boundary plane distributions and single-step versus multiple-step grain boundary engineering. Acta Mater A524:134–142

[31] Ghamarian I, Samimi P, Rohrer GS, Collins PC (2017) Determination of the five parameter grain boundary character distribution of nanocrystalline alpha-zirconium thin films using transmission electron microscopy. Acta Mater 130:164–176

[32] Rohrer GS, Miller HM (2010) Topological characteristics of plane sections of polycrystals. Acta Mater 58:3805–3814

[33] Schuh CA, Kumar M, King WE (2003) Analysis of grain boundary networks and their evolution during grain boundary engineering. Acta Mater 51:687–700

[34] Schuh CA, Minich RW, Kumar M (2003) Connectivity and percolation in simulated grain boundary networks. Philos Mag 83:711–726

[35] Frary M, Schuh CA (2005) Grain boundary network: scaling laws, preferred cluster structure, and their implications for grain boundary engineering. Acta Mater 53:4323–4335

[36] Kobayashi S, Maruyama T, Tsurekawa S, Watanabe T (2012) Grain boundary engineering based on fractal analysis for control of segregation-induced intergranular brittle fracture in polycrystalline nickel. Acta Mater 60:6200–6212

[37] Kobayashi S, Kobayashi R, Watanabe T (2016) Control of grain boundary connectivity based on fractal analysis for improvement of intergranular corrosion resistance in SUS316L austenitic stainless steels. Acta Mater 102:397–405

[38] Watanabe T (1984) An approach to grain boundary design for strong and ductile polycrystals. Res Mechanica 11:47–84

[39] Watanabe T, Tsurekawa S (1999) The control of brittleness and development of desirable mechanical properties in polycrystalline systems by grain boundary engineering. Acta Mater 47:4171–4185

[40] Watanabe T (2011) Grain boundary engineering: historical perspective and future prospects. J Mater Sci 46:4095–4115. https://doi.org/10.1007/s10853-011-5393-z

[41] Watanabe T, Fujii H, Oikawa H, Arai K-I (1989) Grain boundaries in rapidly solidified and annealed Fe-6.5 mass% Si polycrystalline ribbons with high ductility. Acta Metall 37:941–952

[42] Watanabe T, Arai KI, Yoshimi K, Oikawa H (1989) Texture and grain boundary character distribution (GBCD) in rapidly solidified and annealed Fe-6.5mass%Si ribbons. Philos Mag Lett 59:47–52

[43] Kobayashi S, Tsurekawa S, Watanabe T, Kobylanski A (2008) Control of grain boundary microstructures in molybdenum polycrystals by thermomechanical processing of single crystals. Philos Mag 88:489–506

[44] Kobayashi S, Tsurekawa S, Watanabe T (2009) Evolution of grain boundary microstructures in molybdenum by thermomechanical processing from single crystals. Ceram Trans 201:681–692

[45] Bhowmik A, Biswas S, Suwas S, Ray RK, Bhattacharjee D (2009) Evolution of grain boundary microstructure and texture in interstitial-free steel processed by equal-channel angular extrusion. Metall Mater Trans 40A:2729–2742

[46] Tsurekawa S, Kokubun S, Watanabe T (1999) Effect of grain boundary microstructures on brittle fracture in polycrystalline molybdenum. Mater Sci Forum 304–306:687–692

[47] Tsurekawa S, Watanabe T (2000) Grain boundary microstructure-dependent intergranular fracture in polycrystalline molybdenum. Mat Res Soc Symp Proc (Interfacial Eng Optim Prop II) 586:237–242

[48] Zhong Y, Yin F, Sakaguchi T, Nagai K, Yang K (2007) Dislocation structure evolution and characterization in the compression deformed Mn-Cu alloy. Acta Mater 55:2747–2756

[49] Allain-Bonasso N, Wagner F, Berbenni S, Field DP (2012) A study of the heterogeneity of plastic deformation in IF steel by EBSD. Mater Sci Eng A548:56–63

[50] Bouquerel J, Diawara B, Dubois A, Dubar M, Vogt J-B, Najjar D (2015) Investigations of the microstructural response to a cold forging process of the 6082-T6 alloy. Mater Des 68:245–258

[51] Palumbo G, Aust KT (1992) Special properties of Σ grain boundaries. In: Wolf D, Yip S (eds) Materials interfaces: atomic-level structure and properties. Chapman & Hall, London, pp 190–211

[52] Takechi H, Kato H, Nagashima S (1968) Rolling and annealing textures of low-carbon steel sheets. Trans Met Soc AIME 242:56–65

[53] Park YB, Lee DN, Gottstein G (1998) The evolution of recrystallization texture in body centered cubic metals. Acta Mater 46:3371–3379

[54] Humphreys FJ, Hatherly M (1996) Recrystallization and related annealing phenomena. Pergamon, Oxford

[55] Watanabe T (1993) Grain boundary design for advanced materials on the basis of the relationship between texture and grain boundary character distribution (GBCD). Textures Microstruct 20:195–216

[56] Garbacz A, Grabski MW (1989) Modelling of CSL boundaries distribution in polycrystals. Script Metall 23:1369–1374

[57] Gertsman VY, Zhilyaev AP, Pshenichnyuk AI, Valiev RZ (1992) Modelling of grain-boundary misorientation spectrum in polycrystals with crystallographic texture. Acta Metall Mater 40:1433–1441

[58] Garbacz A, Grabski MW (1993) The relationship between texture and CSL boundaries distribution in polycrystalline materials-I. The grain boundary misorientation distribution in random polycrystal. Acta Metall Mater 41:469–473

[59] Garbacz A, Grabski MW (1993) The relationship between texture and CSL boundaries distribution in polycrystalline materials-II. Analysis of the relationship between texture and coincidence grain boundary distribution. Acta Metall Mater 41:475–483

[60] Zuo L, Watanabe T, Esling C (1994) A theoretical approach to grain boundary character distribution (GBCD) in textured polycrystalline materials. Z Metallkde 85:554–558

[61] Thompson AW, Backofen WA (1971) The effect of grain size of fatigue. Acta Metall 19:597–606

[62] Mughrabi H, Höppel HW (2010) Cyclic deformation and fatigue properties of very fine-grained metals and alloys. Int J Fatigue 32:1413–1427